Thickness control of organic semiconductor-incorporated perovskites

Jee Yung Park[1,12], Ruyi Song[2,12], Jie Liang[3,12], Linrui Jin[4,12], Kang Wang[1], Shunran Li[5,6], Enzheng Shi[7], Yao Gao[8], Matthias Zeller[4], Simon J. Teat[9], Peijun Guo[5,6], Libai Huang[4]*, Yong Sheng Zhao[3]*, Volker Blum[2,10]*, Letian Dou[1,4,11]*

[1]Davidson School of Chemical Engineering, Purdue University, West Lafayette, IN 47907, United States.

[2]Department of Chemistry, Duke University, Durham, NC 27708, United States.

[3]Key Laboratory of Photochemistry, Institute of Chemistry, Chinese Academy of Sciences, Beijing 100190, China.

[4]Department of Chemistry, Purdue University, West Lafayette, IN 47907, United States.

[5]Department of Chemical and Environmental Engineering, Yale University, New Haven, CT 06511, United States.

[6]Energy Sciences Institute, Yale University, West Haven, CT 06516, United States.

[7]Research Center for Industries of the Future and School of Engineering, Westlake University, Hangzhou 310030, China.

[8]State Key Laboratory of Material Processing and Die & Mold Technology, School of Materials Science and Engineering, Huazhong University of Science and Technology, Wuhan 430074, China.

[9]Advanced Light Source, Lawrence Berkeley National Laboratory, Berkeley, California 94720, United States.

[10]Thomas Lord Department of Mechanical Engineering and Materials Science, Duke University, Durham, NC 27708, United States.

[11]Birck Nanotechnology Center, Purdue University, West Lafayette, IN 47907, United States.

[12]These authors contributed equally.

*Corresponding authors: E-mail: dou10@purdue.edu (L.D.); volker.blum@duke.edu (V.B.); yszhao@iccas.ac.cn (Y.S.Z.); libai-huang@purdue.edu (L.H.)

Two-dimensional organic semiconductor-incorporated perovskites (OSiP) are a promising family of hybrid materials for optoelectronic applications, owing in part to their inherent quantum well architecture. Tuning their structures and properties for specific properties however has remained challenging. Here we report a general method to tune the dimensionality of phase-pure OSiP single crystals during their synthesis, by judicious choice of solvent. The length of the conjugated semiconducting organic cations and the dimensionality (n value) of the inorganic layers can be manipulated at the same time. The energy band offsets and exciton dynamics at the organic–inorganic interfaces can therefore be precisely controlled. Furthermore, we show that longer and more planar π-conjugated organic cations induce a more rigid inorganic crystal lattice, which leads to suppressed exciton–phonon interactions and better optoelectronic properties as compared to conventional two-dimensional perovskites. As a demonstration, optically driven lasing behavior with substantially lower lasing thresholds was realized.

Two-dimensional (2D) hybrid perovskites have drawn significant interest in recent years for their unique exciton dynamics from inherent quantum wells and controllable optoelectronic properties thanks to their compositional tunability[1–7]. For 2D hybrid perovskites with a general chemical formula $(L)_2(A)_{n-1}M_nX_{3n+1}$, where L is a long chain organic cation, A is a small organic cation such as methylammonium (MA), M is a metal cation such as lead or tin, and X is a halide anion with n being an integer that determines the dimensionality or slab thickness (quantum well thickness), changes in each component provide a viable approach to derive specific optoelectronic properties[8–15]. In early examples of 2D perovskites, the organic species (L) were limited to simple cations such as butyl ammonium (BA) or phenylethyl ammonium (PEA) which act as insulating energy barriers that restrict charge transfer[16,17]. In these systems, the lattice dynamics, exciton dynamics, as well as electronic and mechanical properties of 2D perovskites are constrained by the narrow choice of soft organic molecules.

Recently, 2D organic semiconductor-incorporated perovskites (OSiP) have been demonstrated, in which the insulating barriers were replaced with organic semiconductors[18–21]. Although OSiPs exhibit greatly improved electrical properties and intrinsic stability, studies until now have been limited to the n=1 dimensionality, owing to synthetic challenges for higher n phases. As a result, a clear fundamental understanding on the structure-property relationship is still lacking and the full potential of this exciting new family of hybrid materials has not been realized.

In this work, we demonstrate a crystal growth method to synthesize high-quality dimensionality-controlled OSiP single crystals by introducing a novel solvent system, and we report new structures with different n-values that incorporate oligothiophene-based semiconducting molecules. Hybrid density functional theory (DFT) calculations show that complete tuning of the band alignment between the organic and inorganic building blocks can be achieved in these OSiPs. We further uncover a wide spectrum of underlying exciton behavior through temperature-dependent ultrafast spectroscopy measurements. Intriguingly, our study reveals that π-conjugated molecules allow us to manipulate the rigidity of the crystal lattice and thus control the phonon-exciton coupling. As a result, OSiPs with increased crystal rigidity exhibit a vastly improved lasing performance showing improved characteristics such as a low lasing threshold and stability at high temperature. Our study establishes that extensive control over organic cation design and dimensionality is a powerful additional degree of freedom in hybrid perovskite design that gives rise to unprecedented optoelectronic properties.

Results and Discussion

Synthesis and crystal structures of OSiPs

Semiconducting organic cations with bi-, tri- and quarter-thiophene units connected to an ethyl ammonium group each named 2T, 3T, and 4Tm were chosen to be incorporated in OSiPs where their molecular structures are shown in **Supplementary Fig. 1**. The overall π-conjugation length in each molecule was considered as a design factor to adjust the highest occupied and lowest unoccupied molecular orbitals (HOMO and LUMO) levels for the hybrid layers to effectively form either straddled or staggered energy band alignments. We sought to control the slab thickness of the inorganic layers between arrays of organic moieties between one and three (n=1-3) to investigate the effect of the OSiP quantum well widths and their derivative properties.

Initially we used a slow cooling crystallization scheme utilizing an aqueous solvent system that included both hydroiodic acid and hypo phosphorous acid[24,25,26]. However, these acidic aqueous conditions did not create an environment suitable for dissolving the bulky conjugated organic cation precursors due to their hydrophobicity. Considering the boiling point, polarity index, and the overall miscibility of various organic solvents, we devised a solvent system assisted by organic alcoholic solvents (ethanol and isopropyl alcohol) in addition to the acidic solvents[27]. The lower polarity of the added solvents increased the reactivity of the conjugated organic cations but was moderate enough to be also compatible with the inorganic components. **Supplementary Fig. 2** shows the new solvent system's capability to fully dissolve both organic as well as inorganic precursors.

Furthermore, the presence of alcoholic solvents limits the growth of 3D perovskite phase and phase disproportionation. As typical crystal growth occurs in two steps comprised of nucleation and growth, the initial nucleation step is crucial to deciding the dimensionality of the 2D perovskite crystal. The *n* number during nucleation is dictated by the competition between inorganic layer propagation and the capping of bulky organic cations on to the inorganic layers to inhibit further increase of dimensionality. Introducing alcoholic solvents with mild polarity interferes with this process so that the vertical growth of inorganic layer is slowed, and the capping of organic cation is relatively facilitated, suppressing 3D perovskite impurities, while increasing *n* phase purity. Also, the combination of aqueous HI solvent and the alcoholic anti-solvent inhibits uncontrolled nucleation at elevated temperatures and allows nuclei to go through a prolonged growth step resulting in large sized single crystals with minimal defects. With this new solvent system, we were able to grow up to millimeter scale single crystals. In this work, seven new OSiP crystals were successfully synthesized – $(2T)_2(MA)Pb_2I_7$ (**2T n=2**), $(2T)_2(MA)_2Pb_3I_{10}$ (**2T n=3**), $(3T)_2PbI_4$ (**3T n=1**), $(3T)_2(MA)Pb_2I_7$ (**3T n=2**), $(3T)_2(MA)_2Pb_3I_{10}$ (**3T n=3**), $(4Tm)_2(MA)Pb_2I_7$ (**4Tm n=2**), and $(4Tm)_2(MA)_2Pb_3I_{10}$ (**4Tm n=3**). Several previously reported materials – $(2T)_2PbI_4$ (**2T n=1**) and $(4Tm)_2PbI_4$ (**4Tm n=1**) – were also included in this work for comparison (See **Supplementary Table 1** for detailed crystal growth parameters)[17].

Side views of the crystal structures are shown in **Fig. 1a-c** (for full structure details see **Supplementary Figs. 3-9 and Supplementary Table 5-10).** Compounds **2T n=2**, **2T n=3**, **3T n=1**, **3T n=2**, **3T n=3**, and **4Tm n=2** were prepared using the new solvent system approach and their structures were resolved using single-crystal X-ray diffraction. For **4Tm n=3**, crystals suitable for single crystal X-ray analysis have not yet been obtained, due to limitations in thickness of the bulk crystals and severe twinning. Its structure was deduced using computational approaches (dispersion-corrected semilocal DFT, see Methods for details). Based on the geometry data obtained from the crystal structures, we studied these three series of OSiPs involving the 2T, 3T, and 4Tm organic cations computationally. For these DFT simulations, we transformed the unit cells to align the c axis to be perpendicular to the inorganic layers and used a (2×2) unit cell, containing four lead-halide octahedra, in the (a-b) plane. For 4Tm n=3 whose crystal structures could not yet be experimentally determined, we approximated their unit cells from the *n*=1 system by shifting the organic cations and inserting the additional inorganic layers (**Supplementary Fig. 10**). The energy of the thus obtained theoretical structures as well as the experimental X-ray based structures were minimized using dispersion corrected semilocal DFT and these energetically optimized and relaxed structures were used for comparisons between all structures. For all crystals, the relaxed structures were in excellent agreement with the corresponding experimentally determined structures (see **Supplementary Information Appendix** for lattice parameters and atomic positions from relaxed structures).

To elucidate the influence of the different organic cations and dimensionality on the crystal structures, bond angles and interatomic distances within each unit cell were compared between different compounds. In general, equatorial structural components (i.e. bond distances and angles within each infinite Pb-I layer) showed more pronounced alterations compared to relatively invariable axial components, as the main intervening force from the conjugated organic cations is exerted perpendicularly to the horizontal (a-b) plane of the inorganic perovskite layer[28]. **Fig. 1d** illustrates 3 components compared herein: the equatorial Pb-I-Pb angle, the N-I distance, and the equatorial Pb-Pb distance, shown in a top view structure schematic. To compare the effect of the organic cations, **Fig. 1e** first shows the data for *n*=1 OSiP structures including several reference 2D perovskites previously reported incorporating BA, PEA, and a 2,1,3-benzothiadiazole unit based (BTm) organic cation[17,29,30]. Interestingly, as organic cations become larger and feature more conjugation (from BA to 3T) the organic layers' influence on the inorganic layer increases. The N-I distances become shorter and the equatorial Pb-I-Pb angles become smaller, consistent with increasing rotation of adjacent PbI_6 octahedra with respect to one another. 4Tm and BTm induce less rotation despite their bulkiness, possibly due to intermolecular interactions weakened by the methyl groups. The slab thickness of the inorganic layers also influences the equatorial Pb-I-Pb angles and Pb-Pb distances. This dependence, extracted from the series of relaxed structures, is displayed in **Fig. 1f**. The structural properties of higher *n*-value phases with thicker inorganic slabs trend toward resembling their 3D counterparts. The trend of these parameters based on experimentally resolved structures including $MAPbI_3$, is shown in **Supplementary Fig. 11.**

Quantum well alignments and optical properties

After relaxation of the geometries, spin-orbit coupled hybrid DFT calculations (see Methods for details) were performed to identify the corresponding electronic band structures and the band level alignments as shown in **Fig. 2**. The band structures are formed by the inorganic valence band maximum (VBM) and conduction band minimum (CBM) together with the frontier orbital levels derived from the organic components. On the one hand, as the thickness of the inorganic layers increases, the VBM energy levels significantly increases (taking the core level of each system as a reference), leading to smaller energy gap in the inorganic layer. On the other hand, as the π-conjugation elongates from 2T to 3T and 4Tm, the gap between organic HOMO and LUMO becomes narrower. Taking these two trends into consideration, we observe a transition between type I and type II band alignment. Interestingly, the flexibility in the extent of band offset includes pseudo-type I and pseudo-type II band alignments where the predicted band offset between organic and inorganic VBM components are smaller than a few k_BT.[31] For example, **3T n=1** and **4Tm n=2** quantum wells which show close VBM and HOMO can be considered a pseudo-type II whereas the quantum well of **4Tm n=3** would be a pseudo-type I. Note that in principle the energy levels of both the inorganic and organic moieties can be estimated experimentally using ultraviolet photoelectron spectroscopy (UPS)[32]. However, in practice we found it difficult to produce large area phase-pure thin films for *n*=2 and *n*=3 samples and it is hard to clearly differentiate the contributions from the inorganic and the organic moieties individually using UPS. Thus, UPS measured from BA n=1~3 films and Cyclic Voltammetry data of the organic moieties were acquired to provide rough estimates of energy levels which provide further experimental support for the proposed band alignments (**Supplementary Fig. 13-15**).

We note that the spin-orbit coupled hybrid DFT approach used here provides qualitative predictions of energy level alignments that do not include excitonic effects. Inclusion of excitonic effects from first principles would necessitate higher-level many-body approaches such as the Bethe-Salpeter Equation (BSE) based on the *GW* approximation, but such approaches are currently limited to system sizes that are smaller than the structure sizes between 440 and 952 atoms that we address here.[33] Alternatively, semiempirical multiband effective mass theory could provide estimates of the exciton binding energy for inorganic type I systems and empirical Hamiltonians can also capture the more complex excitonic physics of the organic moiety, but both types of theories have not yet been united in a single framework.[34,35] In several past references, we have, however, observed that the present DFT approach can serve as a predictor of strong photoluminescence associated with type-I quantum well alignment on the inorganic component, vs. weaker photoluminescence associated with different alignment, a correlation that we also observe below.[22,23,31,36]

To further examine the photophysical properties predicted by computational simulation, mechanically exfoliated sheets on either transparent glass or Si/SiO_2 substrates were characterized. **Fig. 3a-c** show the optical microscopy images and the photoluminescence (PL) images from ultraviolet (UV) lamp or 375 nm continuous wave laser excitation. UV lamp was used to excite the comparably large area of the single crystal sheets to show the uniformity and purity of the single crystals produced in this work while 375 nm continuous wave laser was used to acquire images and PL spectra of optically quenched samples (**Supplementary Fig. 16**). PL spectra of the exfoliated sheets are shown in **Fig. 3d-f** and time resolved photoluminescence (TRPL) plots are shown in **Fig. 3g-i**. **2T n=1**, **2T n=2**, and **2T n=3**, respectively. PL lifetime calculated from TRPL plots are also shown in **Supplementary Table 3**. All compounds exhibit sharp PL peaks at 522.1 nm, 575.1 nm, and 620.5 nm corresponding to green, yellow, and red color emissions. This is analogous to what has been reported for type I quantum wells such as BA or PEA based 2D perovskites. **3T n=2** and **3T n=3** showed robust PL indicating their similarities with their 2T counterparts. For the 2T and 3T series, PL lifetimes from thicker inorganic layers were longer due to their weaker exciton binding energies.

Unlike typical type I OSiPs, **3T n=1** and the 4Tm series showed partially quenched PL under UV lamp excitation and much shorter PL lifetimes. This agrees with our band alignment analysis that type II alignment quantum wells result in substantially weaker excitonic emissions due to the allowance of charge transfer across the organic-inorganic interface[37]. While **4Tm n=1** and **4Tm n=2** both showed broad peaks accompanied with a wide shoulder around the peak area which is likely an emissive feature from the organic layer, **3T n=1 and 4Tm n=3** both displayed a weak but narrow emissive peak. In **4Tm n=1** and **4Tm n=2**, a superposition of organic excitonic features and inorganic emission is consistent with the observed features reported earlier.[35] **4Tm n=3** with a pseudo type I alignment also resembles emissive properties of a type I quantum well but the intensity remains weak from charge separation facilitated across the hybrid interface due to close HOMO and VBM energy levels. With increase of the n number in the 4Tm series, the inorganic derived exciton becomes dominant for **4Tm n=3**, which agrees with the transition of band alignment from type II to pseudo type II, and to pseudo type I. These results are in overall good agreement with the DFT-predicted band alignments.

Temperature-dependent PL measurements using pulsed laser spectroscopy were performed to gain insight regarding exciton dynamics at the interfaces (**Supplementary Fig. 17-21**). First, for OSiPs with type II alignment, **4Tm n=1** exhibits new peaks at approximately 630 nm and 830 nm at low temperature while **4Tm n=2** exhibits new peaks in the 700 nm and 770 nm regions. PL lifetimes of **4Tm n=1** through a 600 nm long pass filter (measuring 630 nm and 830 nm) were long-lived compared to the emission from shorter wavelengths. Likewise, **4Tm n=2** emissions through a 700 nm long pass filter show a considerably prolonged lifetime compared to shorter wavelength regions of the PL spectra (**Supplementary Fig. 20**). Increased lifetime of longer wavelength peaks suggests that the low temperature activated spectral features emerge from a different radiative decay pathway other than the common inorganic or organic exciton recombination, which is deemed to be short-lived (see **Supplementary Fig. 22-26** for additional optical characterization results and analysis for OSiPs).

Lattice dynamics and lasing performance

As type I quantum wells, OSiPs of the 2T and 3T series exhibit strong and narrow emissions. The change in lattice dynamics induced by the organic layer can greatly affect the excitonic behavior within, thus altering optical properties. From temperature dependent PL measurements, the **2T n=1** and **2T n=2** emission peaks show a blue shift from room temperature to 126 K where it reverses, and red shifts from 126 K to 6.5 K **(Supplementary Fig. 17a-b)**. This trend is consistent with previous observations from BA based 2D perovskites and is widely associated with the thermal expansion of the 2D perovskite crystal lattice dependent on temperature[38,39]. Nonetheless, **3T n=1** and **3T n=2** show a monotonic blue shift of their PL peaks from room temperature to 6.5K, which is a trend observed for conventional inorganic III-V semiconductors **(Supplementary Fig. 17d-e)**. This observation highlights that 3T makes OSiPs less susceptible to lattice expansion or contraction, most likely due to their longer conjugation length and stronger intermolecular interactions.

These findings led us to further analyze the rigidity of OSiPs from various aspects. The rigidity of crystal structures can be gauged by atomic displacement values of each atom from experimentally solved crystal structures[40]. **Fig. 4a** displays equivalent isotropic displacement parameters of **BA n=2** along with **2T n=2**, **3T n=2**, and **4Tm n=2** crystals. Oligothiophene based 2D perovskites show substantially smaller atomic displacement parameter values compared to BA. Among OSiPs, **3T n=2** shows the least while **4Tm n=2** shows the highest atomic displacement and n=1 OSiPs also display a similar trend **(Supplementary Fig. 12)**. However, effects of static displacive disorder, as well as those of the always-present atomic motion, effects from low quality data, and procedures used during processing of single crystal X-ray data can also contribute to the atomic displacement parameters[41]. Thus, it is noted that atomic displacement must not be overinterpreted and precise quantitative comparisons require caution. To further characterize rigidity, low frequency Raman scattering spectra of **BA n=1**, **2T n=1**, and **3T n=1** was also collected for comparison (**Fig. 4b**). The positions of vibrational bands indicated by each peak were overall red shifted in **2T n=1** with respect to **3T n=1**, while broad peak feature was observed for **BA n=1** at room temperature due to the dynamically disordered BA cations. This observation can be explained by the difference in rigidity of two systems resulting from the relative stiffness of 3T compared to 2T and this is most well displayed in n=1 OSiPs which are relatively more influenced by the organic layer than n=2 OSiPs (**Supplementary Fig. 27**)[42,43]. Additional temperature dependent low frequency Raman spectra can be found in **Supplementary Fig. 28**, which suggest the lack of phase transition in **2T n=1** and **3T n=1** down to 78 K, in contrast to **BA n=1** which exhibits a phase transition near room temperature due to more dynamically disordered BA cations compared to 2T and 3T.[44,45] Furthermore, nanoindentation was conducted to gauge the mechanical rigidity of OSiPs compared to conventional 2D perovskites.[46] Higher values of Young's modulus were obtained for 2T n=1 and n=2 compared to BA n=1 and n=2, also supporting that the trend in macroscopic mechanical rigidity is in alignment with the microscopic structural rigidity as well (**Supplementary Fig. 29**).

The effect of overall rigidity on lattice dynamics can be better monitored by quantifying exciton-phonon interaction through temperature dependent full width at half maximum (FWHM) analysis of the PL spectra.[47] As temperature nears room temperature, PL spectral features exhibit broadened asymmetricity due to phonon scattering and thus, the FWHM is considered as a good approach to compare the extent of thermal broadening and quantify the exciton-phonon coupling strength through fitting of the values. FWHM of a PL emission is expressed by the following equation[48–51]:

$$\boldsymbol{\Gamma(T) = \Gamma_0 + \Gamma_{AC} * T + \frac{\Gamma_{LO}}{exp(\frac{E_{LO}}{k_B T}) - 1}}$$

where $\boldsymbol{\Gamma_0}$ is an inhomogeneous broadening factor, $\boldsymbol{\Gamma_{AC}}$ is the exciton-longitudinal acoustic phonon coupling strength, $\boldsymbol{\Gamma_{LO}}$ is the exciton-longitudinal optical (LO) phonon coupling strength, and $\boldsymbol{E_{LO}}$ is the longitudinal optical phonon energy.

Fig. 4c compares the temperature dependent FWHM of **2T n=1**, **2T n=2**, and **2T n=3**. Since LO phonons are the dominant phonons in polar semiconductors, the acoustic phonon term was neglected in the initial fitting attempts. **2T n=2** and **2T n=3** gave good fitting results with this assumption and LO phonon energy values were also calculated as 0.015 eV and 0.008 eV for **2T n=2** and **2T n=3**, respectively, which is in range with Pb-I-Pb phonon mode values previously reported[50,52]. **2T n=1**, however, showed linear dependence of the FWHM values and was fitted including the acoustic phonon term (**Supplementary Table 4a**). This agrees with previous reports suggesting that unusually strong quantum confinement characteristics in *n*=1 perovskite crystals can lead to increased scattering of charge carriers by acoustic phonons[53,54]. Overall, we observed decreased exciton-phonon coupling strength with increasing n numbers.

Temperature dependent FWHM of the 3T series was also fitted and compared with the 2T series to observe the impact of the organic cations on exciton-phonon coupling. **Fig. 4d-f** shows a temperature dependent FWHM comparison of the 2T and 3T series comparing each n numbers. Overall, we observe reduced thermal broadening for the 3T series signaling a decreased exciton-phonon coupling induced by the rigidified crystal lattice. As *n*=1 is most influenced by the organic cations, it shows the most prominent difference in thermal broadening while as the *n* number increases, the extent of difference decreases.[55] This trend is also quantifiable with fitted values for the LO phonon coupling strength (**Supplementary Table 4**). For comparison of n=2 and n=3 OSiPs incorporating 2T and 3T, the LO phonon energies were fixed based on the **2T n=2** and **n=3** fitting from **Fig. 4c**. Exciton-LO phonon coupling strengths were calculated as 0.066 eV and 0.028 eV for **2T n=2** and **2T n=3** respectively while **3T n=2** and **3T n=3** showed suppressed phonon-exciton coupling with decreased coupling strength values of 0.029 eV and 0.016 eV. It is noted that OSiPs potentially go through a phase transition (**Supplementary Fig. 17**) which can abruptly alter the emission peaks (observed around 50 K) which can influence the overall quality of the FWHM fitting in each dataset differently.

Our findings indicate that intriguingly longer π-conjugated organic cations induce a more rigid inorganic crystal lattice, which leads to suppressed exciton-phonon interactions. This results in improved lasing properties of the OSiPs as compared to conventional two-dimensional perovskites. **Fig. 5a-b** shows the lasing characteristics from exfoliated crystals of **3T n=2** at 10 K under pulsed UV laser excitation. **Fig. 5c** shows the temperature dependent lasing characteristics where **3T n=2** shows stable lasing up to 150 K allowed by relatively smaller exciton-phonon interactions. As seen from **Fig. 5e** which compares pump fluence dependent PL intensity and FWHM of **2T n=3** and **3T n=3** lasing, **3T n=3** with a longer π-conjugation indeed has a lower lasing threshold due to suppressed exciton-phonon coupling.

Additional lasing PL spectra are displayed in **Fig. 5d** in comparison with non-lasing PL peaks and detailed lasing characteristics from **2T n=2**, **2T n=3**, and **3T n=3** as well as the polarization characterization of **3T n=2** can be found in **Supplementary Fig. 30-35**. The temperature dependence of lasing thresholds for each material is summarized in **Fig. 5f**. In agreement with some previous reports[56], we were not able to observe lasing from **BA n=1** and **BA n=2** perovskites. **2T n=2**, **2T n=3** and **3T n=3** showed lasing at a temperature as high as 150 K with substantially lower thresholds compared to their BA counterpart (**Fig. 5f**). The 4Tm series, particularly *n*=3 which has a pseudo type I quantum well alignment was also tested but lasing was not observed. Regarding the *n* value dependence, *n*=3 perovskites exhibit relatively lower thresholds than members of the *n*=2 series. Regarding organic cation dependence, the 3T series exhibits lower thresholds than the 2T series. These results suggest that substantial enhancement in lasing properties can be achieved through rigidifying the 2D OSiP crystal lattice via increasing the quantum well thickness and organic cation design.

Conclusion

In summary, we have devised a general method to synthesize dimensionality-controlled OSiP single crystals utilizing a new solvent system demonstrating that various OSiP quantum wells with desired band alignments can be designed by modulating the conjugated semiconducting organic cations and the dimensionality (*n* value) at the same time. The exciton and lattice dynamics were fully characterized both experimentally and theoretically, unveiling the key contributions of the π-conjugated organic cations in the hybrid structures. Furthermore, we found that OSiPs with π-conjugated organic cations with stronger intermolecular interaction facilitate a more rigid inorganic crystal lattice, which leads to suppression of phonon-electron interactions and improved optoelectronic properties. For example, optically driven stimulated emission from OSiPs were observed with dramatically decreased lasing thresholds compared to conventional 2D perovskites. Our findings expand the horizon in designing and synthesizing new OSiPs for achieving unprecedented optoelectronic properties and potentially allow wide application of 2D perovskites in next-generation optoelectronic devices.

Acknowledgements

We thank D. Mitzi and M. K. Jana for help with single crystal X-ray diffraction studies. We also thank Dr. Kejie Zhao and Xiaokang Wang at School of Mechanical Engineering, Purdue University for the nanoindentation experiments. The work of J.P. and L.D. is supported by the National Science Foundation under award no. 2110706-DMR (crystal synthesis). The work of L.J. and L.H. is supported by U.S. Department of Energy, Office of Basic Energy Sciences under award no. DE-SC0022082 (spectroscopy characterization). The work of R.S. and V.B. is supported by the National Science Foundation under award no. DMR-1729297 (density functional theory calculations). The work of J.L. and Y.S.Z. is supported by the New Cornerstone Science Foundation through the XPLORER PRIZE. This research used resources of the National Energy Research Scientific Computing Center (NERSC); a U.S. Department of Energy (DOE) Office of Science User Facility operated under Contract no. DEAC02-05CH11231. The single-crystal X-ray diffractometer was purchased with support from the National Science Foundation under award no. CHE 1625543. This research used resources of the Advanced Light Source, which is a DOE Office of Science User Facility under contract no. DE-AC02-05CH11231.

Author Contributions

J.P. carried out the synthesis, characterization of the materials, and overall data analysis. R.S. and V.B. performed density functional theory simulations. J.L. and Y.S.Z. characterized the temperature dependent lasing properties of the materials. L.J. and L.H. carried out the temperature dependent ultrafast spectroscopy measurements. K.W. provided insight regarding characterization and overall data analysis. E.S. and Y.G. contributed to synthesis of materials. M.Z. and S.J.T. performed single crystal structure determinations. S.L. and P.G. carried out low frequency Raman scattering measurements. J.P. and L.D. wrote the manuscript; all authors read and revised the manuscript. L.D. supervised the project.

Competing Interests

V.B. is a member of the executive board of MS1P e.V., the non-profit organization which licenses the FHI-aims electronic structure code used in this work. V.B. does not receive any financial gains from this position. L.D. and Y.G. has a pending patent application (Patent Application Number: 20200062740) related to this work. All other authors declare no competing interests.

Additional Information

Supplementary information is available in the online version of the paper. Reprints and permission information is available online at www.nature.com/reprints. Correspondence and requests for materials should be addressed to L.D. or V.B. or Y.S.Z. or L.H.

Figure Captions

Figure 1| Crystal structure characterizations of 2D OSiPs incorporating 2T, 3T, and 4Tm organic cations. a-c, Side view of crystal structures of 2T, 3T, and 4Tm series with n = 1 ~ 3 (from left to right). For **4Tm n=3**, crystal structure was deduced from dispersion corrected semilocal DFT; all other structures displayed are original crystal structures determined from single crystal X-ray diffraction. **d,** Illustration of N-I distance, equatorial Pb-Pb distance, and Pb-I-Pb angle from a top view. **e,** Trend of average N-I distance and equatorial Pb-I-Pb angle among BA, PEA, 2T, 3T, 4Tm, and BTm based n=1 2D perovskites. **f,** Change in average equatorial Pb-I-Pb angle and Pb-Pb distance depending on the dimensionality (n value) analyzed from the DFT-relaxed structures.

Figure 2| DFT calculated electronic structures and band alignments of 2D OSiPs. a-i, (a) 2T n=1, **(b) 2T n=2**, **(c) 2T n=3**, **(d) 3T n=1**, **(e) 3T n=2**, **(f) 3T n=3**, **(g) 4Tm n=1**, **(h) 4Tm n=2**, and **(i) 4Tm n=3** with different inorganic layer thickness and organic components. The left side of each panel shows HSE06 + SOC band structures of the 2D hybrid perovskite systems. The inorganic derived frontier states are mainly contributed by the Pb and I atoms (highlighted in purple and green, respectively). The Pb 1s core energies are aligned to -

97687.486 eV for a better comparison of frontier bands and the bandgap values are shown in each plot. The right side of each panel displays the inorganic and organic band level alignments within each 2D hybrid perovskite system studied here. Type I and type II band alignments are denoted by blue and red shades on the right side of each panel. More transparent shades represent closer HOMO and VBM levels.

Figure 3| Optical images and spectroscopic studies of mechanically exfoliated 2D OSiP single crystals. a-c, (a) 2T, **(b)** 3T, and **(c)** 4Tm series deposited on SiO2/Si. PL images of quenched nanosheets with low PL intensity were also measured with continuous wave laser excitation (red dotted square area). **d-f,** PL spectra gathered from corresponding exfoliated crystals of **(d)** 2T, **(e)** 3T, and **(f)** 4Tm. As **3T n=1** showed substantially weaker PL intensity than **3T n=2** and **3T n=3**, numbers beside each emission peaks indicate the peak intensity multiplied for normalization. For quenched 4Tm series the PL spectra were gathered through concentrated excitation on a single nanosheet from a continuous UV laser beam. **g-i,** TRPL measured through ultrafast spectroscopy from **(g)** 2T, **(h)** 3T, and **(i)** 4Tm series.

Figure 4| Quantification of crystal rigidity and exciton-phonon interactions. a, Equivalent isotropic displacement parameters extracted from single crystal XRD measurements of **BA n=2**, **2T n=2**, **3T n=2**, and **4Tm n=2** bulk crystals. **b,** Low-frequency Raman spectrum of **BA n=1**, **2T n=1** and **3T n=1** at room temperature. **c-f,** Temperature dependent FWHM values of **(c)** 2T series compared, **(d) 2T n=1** and **3T n=1** compared, **(e) 2T n=2** and **3T n=2** compared, and **(f) 2T n=3** and **3T n=3** compared along with fitted lines (dotted lines) measured from 6 K to 205 K. $\boldsymbol{\Gamma_{AC}}$, exciton-longitudinal acoustic phonon coupling strength or $\boldsymbol{\Gamma_{LO}}$, exciton-longitudinal optical phonon coupling strength calculated from the fitting are also compared.

Figure 5| Lasing properties of rigidified OSiP crystal lattices. a-c, Lasing characteristics of **3T n=2** showing **(a)** lasing spectra at 10 K with pump fluence of 140, 280, 560, and 700 nJ/cm^2 (inset: bright-field and lasing images of the crystal, scale bar: 10 μm), **(b)** pump fluence dependent PL intensity and FWHM, and **(c)** temperature dependent lasing PL spectra from 30 K to 150 K. Selective and strong amplification of several mode peaks were observed when the pump fluence reached around 280 nJ/cm^2 at 10 K. Above the onset power for each temperature, FWHM dramatically narrowed down to less than 1 nm and the peak intensity showed nonlinear increase with the pump fluence, exhibiting a clear knee behavior and threshold characteristic indicative of lasing. **d,** Lasing and PL spectra of BA, 2T, and 3T series from *n*=1 to *n*=3 where **BA n=3**, **2T n=2**, **2T n=3**, **3T n=2**, and **3T n=3** exhibits lasing **e,** Pump fluence dependent PL intensity and FWHM comparison of **2T n=3** and **3T n=3**. **f,** Comparison of temperature dependent lasing pump thresholds of different OSiPs.

References:

1. Ishihara, T., Takahashi, J. & Goto, T. Exciton state in two-dimensional perovskite semiconductor (C10H21NH3)2PbI4. *Solid State Commun.* **69**, 933–936 (1989).
2. Katan, C., Mercier, N. & Even, J. Quantum and Dielectric Confinement Effects in Lower-Dimensional Hybrid Perovskite Semiconductors. *Chem. Rev.* **119**, 3140–3192 (2019).
3. Tsai, H. *et al.* High-efficiency two-dimensional ruddlesden-popper perovskite solar cells. *Nature* **536**, 312–317 (2016).
4. Wang, N. *et al.* Perovskite light-emitting diodes based on solution-processed self-organized multiple quantum wells. *Nat. Photonics* **10**, 699–704 (2016).
5. Zhang, Q., Chu, L., Zhou, F., Ji, W. & Eda, G. Excitonic Properties of Chemically Synthesized 2D Organic–Inorganic Hybrid Perovskite Nanosheets. *Adv. Mater.* **30**, 1–8 (2018).
6. Blancon, J., Even, J., Stoumpos, C. C., Kanatzidis, M. G. & Mohite, A. D. Semiconductor physics of organic–inorganic 2D halide perovskites. *Nat. Nanotechnol.* **15**, (2020).
7. Dou, L. *et al.* Atomically thin two-dimensional Organic-inorganic hybrid perovskites. *Science (80-.).* **349**, 1518–1521 (2015).
8. Mitzi, D. B. Templating and structural engineering in organic-inorganic perovskites. *J. Chem. Soc. Dalt. Trans.* 1–12 (2001) doi:10.1039/b007070j.
9. Saparov, B. & Mitzi, D. B. Organic-Inorganic Perovskites: Structural Versatility for Functional Materials Design. *Chem. Rev.* **116**, 4558–4596 (2016).
10. Leng, K., Fu, W., Liu, Y., Chhowalla, M. & Loh, K. P. From bulk to molecularly thin hybrid perovskites. *Nat. Rev. Mater.* (2020) doi:10.1038/s41578-020-0185-1.
11. Shi, E. *et al.* Two-dimensional halide perovskite nanomaterials and heterostructures. *Chem. Soc. Rev.* **47**, 6046–6072 (2018).
12. Ricciardulli, A. G., Yang, S., Smet, J. H. & Saliba, M. Emerging perovskite monolayers. *Nat. Mater.* (2021) doi:10.1038/s41563-021-01029-9.

13. Hu, J., Yan, L. & You, W. Two-Dimensional Organic–Inorganic Hybrid Perovskites: A New Platform for Optoelectronic Applications. *Adv. Mater.* **30**, (2018).
14. Raghavan, C. M. *et al.* Low-Threshold Lasing from 2D Homologous Organic-Inorganic Hybrid Ruddlesden-Popper Perovskite Single Crystals. *Nano Lett.* **18**, 3221–3228 (2018).
15. Zhang, H. *et al.* 2D Ruddlesden–Popper Perovskites Microring Laser Array. *Adv. Mater.* **30**, 1–8 (2018).
16. Zhang, F. *et al.* Enhanced Charge Transport in 2D Perovskites via Fluorination of Organic Cation. *J. Am. Chem. Soc.* **141**, 5972–5979 (2019).
17. Xiao, X. *et al.* Ultrafast Exciton Transport with a Long Diffusion Length in Layered Perovskites with Organic Cation Functionalization. *Adv. Mater.* **32**, 1–9 (2020).
18. Gao, Y. & Dou, L. Organic semiconductor-incorporated two-dimensional halide perovskites. *Natl. Sci. Rev.* (2021).
19. Chondroudis, K. & Mitzi, D. B. Electroluminescence from an organic-inorganic perovskite incorporating a quaterthiophene dye within lead halide perovskite layers. *Chem. Mater.* **11**, 3028–3030 (1999).
20. Mitzi, D. B., Chondroudis, K. & Kagan, C. R. Design, structure, and optical properties of organic-inorganic perovskites containing an oligothiophene chromophore. *Inorg. Chem.* **38**, 6246–6256 (1999).
21. Takeoka, Y., Asai, K., Rikukawa, M. & Sanui, K. Incorporation of conjugated polydiacetylene systems into organic—inorganic quantum-well structures. *Chem. Commun.* **1**, 2592–2593 (2001).
22. Gao, Y. *et al.* Molecular engineering of organic–inorganic hybrid perovskites quantum wells. *Nat. Chem.* **11**, 1151–1157 (2019).
23. Liu, C. *et al.* Tunable Semiconductors: Control over Carrier States and Excitations in Layered Hybrid Organic-Inorganic Perovskites. *Phys. Rev. Lett.* **121**, 146401 (2018).
24. Mao, L. *et al.* Seven-Layered 2D Hybrid Lead Iodide Perovskites. *Chem* **5**, 2593–2604 (2019).
25. Stoumpos, C. C. *et al.* Ruddlesden-Popper Hybrid Lead Iodide Perovskite 2D Homologous Semiconductors. *Chem. Mater.* **28**, 2852–2867 (2016).
26. Oswald, I. W. H., Koegel, A. A. & Neilson, J. R. General Synthesis Principles for Ruddlesden-Popper Hybrid Perovskite Halides from a Dynamic Equilibrium. *Chem. Mater.* **30**, 8606–8614 (2018).

27. Snyder, L. R. Classification off the solvent properties of common liquids. *J. Chromatogr. Sci.* **16**, 223–234 (1978).
28. Mao, L. *et al.* Hybrid Dion-Jacobson 2D Lead Iodide Perovskites. *J. Am. Chem. Soc.* **140**, 3775–3783 (2018).
29. Mitzi, D. B. Synthesis , Crystal Structure , and Optical and Thermal Properties of $(C_4H_9NH_3)_2MI_4$ (M = Ge, Sn, Pb). *Chem. Mater.* 8, 3, 791–800 (1996).
30. Du, K. Z. *et al.* Two-Dimensional Lead(II) Halide-Based Hybrid Perovskites Templated by Acene Alkylamines: Crystal Structures, Optical Properties, and Piezoelectricity. *Inorg. Chem.* **56**, 9291–9302 (2017).
31. Dunlap-Shohl, W. A. *et al.* Tunable internal quantum well alignment in rationally designed oligomer-based perovskite films deposited by resonant infrared matrix-assisted pulsed laser evaporation. *Mater. Horizons* **6**, 1707–1716 (2019).
32. Silver, S., Dai, Q., Li, H., Brédas, J. L. & Kahn, A. Quantum Well Energetics of an n = 2 Ruddlesden–Popper Phase Perovskite. *Adv. Energy Mater.* **9**, 1–7 (2019).
33. Ammirati, G. *et al.* Band Structure and Exciton Dynamics in Quasi-2D Dodecylammonium Halide Perovskites. *Adv. Opt. Mater.* (2023) doi:10.1002/adom.202201874.
34. Steger, M. *et al.* On the optical anisotropy in 2D metal-halide perovskites. *Nanoscale* **14**, 752–765 (2022).
35. Janke, S. M., Qarai, M. B., Blum, V. & Spano, F. C. Frenkel-Holstein Hamiltonian applied to absorption spectra of quaterthiophene-based 2D hybrid organic-inorganic perovskites. *J. Chem. Phys.* **152**, (2020).
36. Jana, M. K. *et al.* Resolving rotational stacking disorder and electronic level alignment in a 2d oligothiophene-based lead iodide perovskite. *Chem. Mater.* **31**, 8523–8532 (2019).
37. Deng, S. *et al.* Long-lived charge separation in two-dimensional ligand-perovskite heterostructures. *J. Chem. Phys.* **152**, (2020).
38. Wang, S. *et al.* Temperature-Dependent Band Gap in Two-Dimensional Perovskites: Thermal Expansion Interaction and Electron-Phonon Interaction. *J. Phys. Chem. Lett.* **10**, 2546–2553 (2019).
39. Yu, C. *et al.* Temperature dependence of the band gap of perovskite semiconductor compound CsSnI3. *J. Appl. Phys.* **110**, (2011).
40. Gong, X. *et al.* Electron-phonon interaction in efficient perovskite blue emitters. *Nat.*

Mater. **17**, 550–556 (2018).

41. Trueblood, K. N. *et al.* Atomic displacement parameter nomenclature report of a subcommittee on atomic displacement parameter nomenclature. *Acta Crystallogr. Sect. A Found. Crystallogr.* **52**, 770–781 (1996).
42. Dhanabalan, B. *et al.* Directional Anisotropy of the Vibrational Modes in 2D-Layered Perovskites. *ACS Nano* **14**, 4689–4697 (2020).
43. Quan, L. N. *et al.* Vibrational relaxation dynamics in layered perovskite quantum wells. *Proc. Natl. Acad. Sci. U. S. A.* **118**, 1–7 (2021).
44. Menahem, M. *et al.* Strongly Anharmonic Octahedral Tilting in Two-Dimensional Hybrid Halide Perovskites. *ACS Nano* **15**, 10153–10162 (2021).
45. Barman, S., Venkataraman, N. V., Vasudevan, S. & Seshadri, R. Phase transitions in the anchored organic bilayers of long-chain alkylammonium lead iodides (CnH2n+1NH3)2PbI4; n = 12, 16, 18. *J. Phys. Chem. B* **107**, 1875–1883 (2003).
46. Tu, Q. *et al.* Out-of-Plane Mechanical Properties of 2D Hybrid Organic-Inorganic Perovskites by Nanoindentation. *ACS Appl. Mater. Interfaces* **10**, 22167–22173 (2018).
47. Du, Q. *et al.* Stacking Effects on Electron-Phonon Coupling in Layered Hybrid Perovskites via Microstrain Manipulation. *ACS Nano* **14**, 5806–5817 (2020).
48. Lee, Koteles & Vassell. Luminiscence linewidths of excitons in GaAs QW below 150. *Phys. Rev. A* **33**, 5512 (1986).
49. Handa, T., Aharen, T., Wakamiya, A. & Kanemitsu, Y. Radiative recombination and electron-phonon coupling in lead-free C H3 N H3Sn I3 perovskite thin films. *Phys. Rev. Mater.* **2**, 1–9 (2018).
50. Ni, L. *et al.* Real-Time Observation of Exciton-Phonon Coupling Dynamics in Self-Assembled Hybrid Perovskite Quantum Wells. *ACS Nano* **11**, 10834–10843 (2017).
51. Chen, Z. *et al.* Remote phononic effects in epitaxial ruddlesden-popper halide perovskites. *J. Phys. Chem. Lett.* **9**, 6676–6682 (2018).
52. Straus, D. B. *et al.* Direct Observation of Electron-Phonon Coupling and Slow Vibrational Relaxation in Organic-Inorganic Hybrid Perovskites. *J. Am. Chem. Soc.* **138**, 13798–13801 (2016).
53. Guo, P. *et al.* Cross-plane coherent acoustic phonons in two-dimensional organic-inorganic hybrid perovskites. *Nat. Commun.* **9**, (2018).
54. Maity, P. *et al.* Layer-Dependent Coherent Acoustic Phonons in Two-Dimensional

Ruddlesden-Popper Perovskite Crystals. *J. Phys. Chem. Lett.* **10**, 5259–5264 (2019).

55. Long, H. *et al.* Exciton-phonon interaction in quasi-two dimensional layered (PEA)2(CsPbBr3): N -1PbBr4 perovskite. *Nanoscale* **11**, 21867–21871 (2019).

56. Liang, Y. *et al.* Lasing from Mechanically Exfoliated 2D Homologous Ruddlesden–Popper Perovskite Engineered by Inorganic Layer Thickness. *Adv. Mater.* **31**, 1–8 (2019).

Methods

Synthesis of the semiconducting conjugated organic cations:

All reactions susceptible to exposure to air and water were conducted under an inert argon atmosphere using a Schlenk line apparatus, employing either tubes or flasks. MA HI was obtained from Greatcell Solar Ltd. All other chemical reagents and solvents were purchased from Sigma Aldrich and used without further purification. Organic intermediates were synthesized following established literature procedures[57–61]. Of the three types of semiconducting organic cations investigated, 2T and 4Tm were synthesized based on methods outlined in our previous study[21], while 3T was prepared using the procedure described below.

General method for the synthesis of Boc protected organic molecules:

A mixture containing tert-Butyl(2-(5-bromothiophen-2-yl)ethyl)carbamate (612 mg, 2 mmol), $Pd_2(dba)_3$ (37 mg, 2 mol%), $P(o\text{-}tol)_3$ (49 mg, 8 mol%), and the corresponding organotin reagent (2.2 mmol) was combined in a Schlenk tube. After purging the tube with argon, toluene (20 mL) was introduced using a syringe. The resulting mixture was stirred at 100 °C for 0.5 hours. Upon cooling to room temperature, water was added, and the mixture was subjected to dichloromethane (DCM) extraction. The combined organic layers were washed with brine, dried with magnesium sulfate, and filtered to remove any solids. The solvents were subsequently removed under vacuum using a rotary evaporator, and the remaining residue was subjected to chromatography on a silica gel column, following the procedure described below.

tert-Butyl(2-([2,2':5',2''-terthiophen]-5-yl)ethyl)carbamate (3T-Boc): The unrefined product underwent purification through column chromatography, using a mixture of dichloromethane and hexane (in a ratio of 1:1) as the solvent for elution. Colorless liquid (75 %). ^{1}H NMR (400 MHz, Chloroform-d) δ 7.21 (dd, J = 5.1, 1.2 Hz, 1H), 7.16 (dd, J = 3.5, 1.2 Hz, 1H), 7.06 (d, J = 3.8 Hz, 1H), 7.03-6.98 (m, 3H), 6.74 (d, J = 3.6 Hz, 1H), 4.69 (s, 1H), 3.41 (d, J = 6.5 Hz, 2H), 2.99 (t, J = 6.7 Hz, 2H), 1.45 (s, 9H).

^{13}C NMR (101 MHz, Chloroform-d) δ 155.67, 140.88, 137.05, 136.23, 135.77, 135.50, 127.76, 126.09, 124.30, 124.17, 123.75, 123.51, 123.46, 79.36, 41.72, 30.60, 28.31.

HR-MS (ESI) Expected 391.07289 $[M]^+$ Observed 391.07253

General method for the synthesis of ammonium salts (3T-HI): The corresponding molecule protected with Boc group (1 mmol) was dissolved in 20 mL of ethanol, and an aqueous solution of HI (2 mmol) was subsequently added. This resulted in the removal of the Boc protecting group and the formation of ammonium iodides in situ at a temperature of 80 °C. The solvents were then evaporated under vacuum. To the resulting residue, diethyl ether was added, and the solid products were collected through filtration and washed multiple times with diethyl ether. The products were finally dried under vacuum for future utilization.

white powder (92 %). ^{1}H NMR (400 MHz, DMSO-d_6) δ 7.79 (s, 3H), 7.51 (dd, J = 5.1, 1.2 Hz, 1H), 7.31 (dd, J = 3.6, 1.2 Hz, 1H), 7.24 (d, J = 3.8 Hz, 1H), 7.19 (d, J = 3.7 Hz, 2H), 7.08 (dd, J = 5.1, 3.6 Hz, 1H), 6.94 (d, J = 3.6 Hz, 1H), 3.13-3.02 (m, 5H).

^{13}C NMR (101 MHz, DMSO-d6) δ 139.06, 136.27, 135.53, 135.12, 128.81, 127.84, 126.08, 125.26, 124.99, 124.60, 27.77.

HR-MS (ESI) Expected 292.02829 $[M – I]^+$ Observed 292.02800

Single crystal growth of organic semiconductor incorporated perovskites (OSiP):

Bulk single crystals were obtained through slow cooling crystallization using a solution composed of hydroiodic acid (HI, wt% in H_2O), hypophosphorous acid (H_3PO_2, wt% H_2O). The alcoholic solvents isopropyl alcohol (C_3H_8O), or ethanol (C_2H_6O) were added to assist dissolution of the organic cations and crystallization. Precursor solutes for semiconducting organic components, 2T HI, 3T HI, or 4Tm HI were mixed with PbI_2 and MAHI in the acidic solution prepared. (See Supplementary Table 1 for detailed crystal growth parameters such as the ratio of solvents and the concentration of each precursor).

After mixing the precursors and solution, the contents of the sample vial were magnetically stirred and heated to 100°C in a water bath until materials were completely dissolved and the solution was clear. The vials were then moved to a Dewar flask water bath at 100°C to cool down for 72 hours until it reached room temperature. With this process, mm scale single crystals were obtained, usually in the form of thin plates or flakes. The crystals were further retrieved from the solution through vacuum filtration for further use. Samples for single crystal structure determination were left in solution until analysis. For n=1 OSiP crystals, a solvent-antisolvent diffusion method was also used to obtain quality single crystals.

Preparation of exfoliated OSiP sheets:

A small number of bulk crystals obtained through single crystal growth were attached to scotch tape and a second scotch tape was pressed on to the crystals. Then, the scotch tapes were peeled off from each other to exfoliate thin sheets from the bulk crystals. This process was repeated

3~4 times. Then, the second scotch tape was attached and pressed onto either a transparent glass or a Si/SiO_2 substrate. The substrates with the scotch tape were left alone on a hotplate at 40°C for 5 mins to ensure deposition of the exfoliated crystals onto the substrate. The scotch tape was then removed.

Single crystal X-ray diffraction:

Single crystal data were collected using a Bruker Quest diffractometer with a fixed chi angle, a sealed tube fine focus X-ray tube, single crystal curved graphite incident beam monochromator, and either a Photon100 (**2T n=2**, **3T n=1**) or a Photon II area detector area detector (**2T n=3**, **3T n=2**, **4Tm n=2**). Instruments were equipped with an Oxford Cryosystems low temperature device and examination and data collection were performed with Mo Kα radiation (λ = 0.71073 Å) at either 150 or 273 K.

Single crystal data for **3T n=3** was collected using Bruker D8 with PHOTONII detector. Data collection was performed at 150 K with radiation (λ = 0.7288 Å) source from the Advanced Light Source synchrotron beamline 12.2.1.

Further details for the reported crystal structures are given in the supplementary tables and related discussions section (**Supplementary Table 5-10**).

Optical microscopy measurements:

All bright-field images were collected with a custom Olympus BX53 microscope. All PL images were taken using a X-Cite Series 120 Q lamp as the excitation source. A coherent continuous wave OBIS 375 nm laser excitation source was used for PL spectrum measurements of quenched samples. PL spectra were collected with a SpectraPro HRS-300 spectrometer.

Temperature dependent photoluminescence (PL) and time-resolved photoluminescence (TRPL):

A home-built PL microscope coupled with a cryostation (Montana s50) were used to conduct temperature dependent PL and TRPL measurements. A 447 nm picosecond pulsed beam (40 MHz) was used as the excitation source, and a pulse picker was adopted to adjust the repetition rate. The beam was focused onto the sample in the cryostation by using a 40× objective (Nikon, NA = 0.6). The emission was collected by the same objective and filtered by a long pass filter. To measure PL spectra, the emission was guided and focused to a spectrometer (Andor Shamrock 303i) and CCD (Andor Newton 920). For TRPL measurements, the emission was alternatively guided and focused to a single photon avalanche diode (PicoQuant, PDM series) with a single photon counting module (PicoQuant).

Micro absorption measurements:

A home-built microscope was used for micro-absorption measurements[62]. Briefly, a halogen tungsten lamp was used as white light source which was focused by an objective (20×, NA = 0.45, Olympus) to a spot with size of ~2 μm on the sample. The transmitted light was collected by anther objective (40×, NA = 0.6, Nikon), and detected by a spectrometer (Andor Shamrock 303i) and CCD (Andor Newton 920).

Transient absorption measurements:

Transient absorption spectra of the single crystals were measured using a home-built femtosecond pump-probe system described in a previous publication[63]. Briefly, the broad-band probe beam was created by focusing the 1030 nm fundamental light (750 kHz, PHAROS, Light Conversion Ltd.) onto a YAG crystal. The wavelength tunable pump was generated from an optical parametric amplifier (ORPHEUS-Twins, Light Conversion Ltd.), and then modulated by a chopper (MC200B, Thorlabs) with a frequency of 195 Hz. A linear stepper motor stage (Newport) was used to delay the probe beam by as much as 800 ps relative to the pump beam. Both pump and probe beams were focused on the sample with a 20× objective (N.A. = 0.45, Olympus). The pump induced change in the probe transmission was collected by another 20× objective (N.A. = 0.45, Olympus) and detected by an array detector (Exemplar LS, B&W Tek).

Optically driven lasing measurements:

The optically pumped lasing measurements for all 2D perovskites were conducted on a homemade micro-photoluminescence system equipped with a cryostat (ST500, Janis) for temperature-dependent characterization. The excitation pulses (400 nm) were generated from a regenerative amplifier (Spitfire, Spectra Physics, 800 nm, 200 fs, 1 kHz), which was in turn seeded by a mode-locked Ti: sapphire laser (Mai Tai, Spectra Physics, 800 nm, 120 fs, 80 MHz). The excitation laser was focused down to a 10 μm diameter spot through an objective lens (Olympus LMPLFLN, 20 ×, N.A. = 0.5). The power at the input was altered by a neutral density filter. The emissions from the individual microcrystal were collected by the same objective in a back-scattering configuration and analyzed by a spectrometer (Princeton Instruments, Acton SpectraPro® SP-2300, spectral resolution < 0.03 nm) equipped with a thermal-electrically cooled CCD (Princeton Instruments, PIX-100BX) after removing the excitation beam with a 450-nm long-pass filter.

Lasing Polarization characterization: The polarization ratio was obtained from the lasing spectra recorded at different rotation angle of a polarizer placed in the front of the spectrometer.

Raman Spectra:

Low-frequency Raman spectra were measured using a frequency-stabilized 785 nm laser (Toptica) as the excitation source with an incident power of 40 mW onto the sample. A set of 5 narrow-linewidth notch filters (OptiGrate) was used to reject the laser line and enable measurements of Raman signatures down to 5 cm^{-1}. A super-long-working-distance objective lens (10x, NA=0.28) was used to focus the excitation light and to collect the Raman signal. The Raman signal was spatially filtered by a pair of 75-mm achromatic lens and a 50-μm pinhole, before sent into the spectrograph (Andor Kymera 328i). The Raman signal was finally captured by a Si EMCCD (Andor iXon Life 888).

Mechanical nanoindentation: Nanoindentation experiments were performed using a KLA G200 Nano-indenter with a Berkovich tip in an argon filled glovebox. Continuous stiffness measurement was implemented on freshly exfoliated surfaces of single crystal samples (>10 μm). Elastic moduli were obtained as the average value for tip penetration from 400 nm to 1000 nm.

NMR Spectra:

NMR spectra were acquired at room temperature with a Bruker AV 400-MHz spectrometer using $CDCl_3$ or d-DMSO as the solvent and tetramethylsilane (TMS) as an internal standard.

Mass Spectrometry:

High resolution mass spectrometry data were acquired in positive electrospray mode (ESI) on an LTQ Orbitrap XL instrument (Thermo Fisher Scientific).

Cyclic Voltammetry:

Solution CV were measured using a CHI660 electrochemical analyzer with a three-electrode cell at a scan rate of 100 mV/s in anhydrous dichloromethane (DCM) with tetrabutylammonium hexafluorophosphate (Bu_4NPF_6, 0.1 mol/L) as the supporting electrolyte. A platinum wire with 2 mm diameter, a Pt wire, and an Ag/AgCl (standard) were used as working, counter and reference electrodes, respectively.

Ultraviolet photoelectron spectroscopy (UPS):

Thin films of the samples were spin-casted onto gold-coated SiO_2/Si substrates. UPS data were obtained using a Kratos Axis Ultra DLD spectrometer with He I radiation (21.2 eV) at a pass energy (PE) of 5 eV. Samples were clamped on a stainless-steel sample holder bar. No cleaning or heating of samples was done in the XPS chamber prior to analysis.

First-principles Calculations:

The first-principles density-functional theory (DFT) simulations were performed using the all-electron electronic structure code package FHI-aims[64]. All calculations are based on the numeric atom-centered orbital (NAO) basis sets. The full relaxation of unit cells and atomic coordinates (all forces on atoms and lattice vectors below 5×10^{-3} eV/Å) were performed with the semilocal Perdew-Burke-Ernzerhof (PBE) functional plus the Tkatchenko-Scheffler (TS) pairwise dispersion scheme[65,66] and FHI-aims "tight" numerical defaults. K-point grids were chosen from (3×3×3), (3×3×2) and (3×3×1), depending on the lattice vector length along the stacking direction of each system. Afterwards, we calculated the electronic properties of these relaxed structure based on the Heyd-Scuseria-Ernzerhof (HSE06) hybrid density-functional[67,68] (with 25% screened exact exchange and a screening parameter of 0.11 (Bohr radii)$^{-1}$)[69] plus second-variation non-self-consistent spin-orbit coupling (SOC).[70] FHI-aims "intermediate" numerical settings and k-point grid (3×3×3) were used. This set of methods was shown to provide a good balance between computational cost and accuracy for hybrid organic-inorganic perovskite systems in our previous studies.[22,23,31,36]

As noted in the main text, this level of theory does not include excitonic effects. Fundamental band gaps of typical hybrid perovskites are underestimated by several tenths of an eV,[23,34] in line with the known uncertainty of HSE06+SOC in the wider community.[71] One way to rationalize the observed ability of this approach to qualitatively predict quantum-well like band alignments in layered perovskites as observed by PL (at least to distinguish inorganic-derived type I vs. type II quantum wells) is that several possible systematic errors, such as in fundamental gap estimates or those associated with exciton binding energies, cancel in differences between energies associated with the organic and inorganic component.

Simulation of electric field intensity distribution:

The electric field intensity distribution in the 3T (n=2) crystal was calculated by using the commercial software COMSOL.

Data and Materials Availability

Crystallographic data for the structures reported in this Article have been deposited at the Cambridge Crystallographic Data Centre under deposition numbers CCDC 2151387 [$(2T)_2(MA)Pb_2I_7$], CCDC 2151388 [$(2T)_2(MA)_2Pb_3I_{10}$], CCDC 2151389 [$(3T)_2PbI_4$], CCDC 2151390 [$(3T)_2(MA)Pb_2I_7$], CCDC 2151391 [$(4Tm)_2(MA)Pb_2I_7$], and CCDC 2191050 [$(3T)_2(MA)_2Pb_3I_{10}$]. Crystallographic data can be obtained free of charge through https://www.ccdc.cam.ac.uk/structures/. All the input and output files relevant to the theoretical simulations in this work have been deposited to the NOMAD, access the following for more information: DOI:10.17172/NOMAD/2023.03.18-1. All other data are available in the manuscript or supplementary information. All materials are available upon request to L.D.

Methods References

57. Guthrie, D. A. & Tovar, J. D. Conformation as a protecting group: A regioselective aromatic bromination en route to complex π-electron systems. *Org. Lett.* **10**, 4323–4326 (2008).

58. Balandier, J. Y. *et al.* Synthesis of soluble oligothiophenes bearing cyano groups, their optical and electrochemical properties. *Tetrahedron* **66**, 9560–9572 (2010).

59. Harvey, C. P. & Tovar, J. D. Pi-conjugated chain extenders for the synthesis of optoelectronic segmented polyurethanes. *J. Polym. Sci. Part A Polym. Chem.* **49**, 4861–4874 (2011).

60. Wang, X. X. *et al.* Dipyrido[3,2-a:2′,3′-c]phenazine-based donor-acceptor aromatic heterocyclic compounds with thienyl and triphenylamino chromophores at the 2,7- and/or 10,13-positions. *Chem. - An Asian J.* **9**, 514–525 (2014).

61. Keller, N. *et al.* Oligothiophene-Bridged Conjugated Covalent Organic Frameworks. *J. Am. Chem. Soc.* **139**, 8194–8199 (2017).

62. Deng, S. *et al.* Long-range exciton transport and slow annihilation in two-dimensional hybrid perovskites. *Nat. Commun.* **11**, 1–8 (2020).

63. Wang, K. *et al.* Lead-Free Organic-Perovskite Hybrid Quantum Wells for Highly Stable Light-Emitting Diodes. *ACS Nano* **15**, 6316–6325 (2021).

64. Blum, V. *et al.* Ab initio molecular simulations with numeric atom-centered orbitals. *Comput. Phys. Commun.* **180**, 2175–2196 (2009).

65. Perdew, J. P., Burke, K. & Ernzerhof, M. Generalized gradient approximation made simple. *Phys. Rev. Lett.* **77**, 3865–3868 (1996).

66. Tkatchenko, A. & Scheffler, M. Accurate molecular van der Waals interactions from ground-state electron density and free-atom reference data. *Phys. Rev. Lett.* **102**, 6–9 (2009).

67. Heyd, J., Scuseria, G. E. & Ernzerhof, M. Hybrid functionals based on a screened Coulomb potential. *J. Chem. Phys.* **118**, 8207–8215 (2003).

68. Heyd, J., Scuseria, G. E. & Ernzerhof, M. Erratum: Hybrid functionals based on a screened Coulomb potential (Journal of Chemical Physics (2003) 118 (8207)). *J. Chem. Phys.* **124**, 2005–2006 (2006).

69. Krukau, A. V., Vydrov, O. A., Izmaylov, A. F. & Scuseria, G. E. Influence of the exchange screening parameter on the performance of screened hybrid functionals. *J. Chem. Phys.* **125**, (2006).

70. Huhn, W. P. & Blum, V. One-hundred-three compound band-structure benchmark of post-self-consistent spin-orbit coupling treatments in density functional theory. *Phys. Rev. Mater.* **1**, 1–18 (2017).

71. Kim, S. *et al.* A band-gap database for semiconducting inorganic materials calculated with hybrid functional. *Sci. Data* **7**, 1–6 (2020).

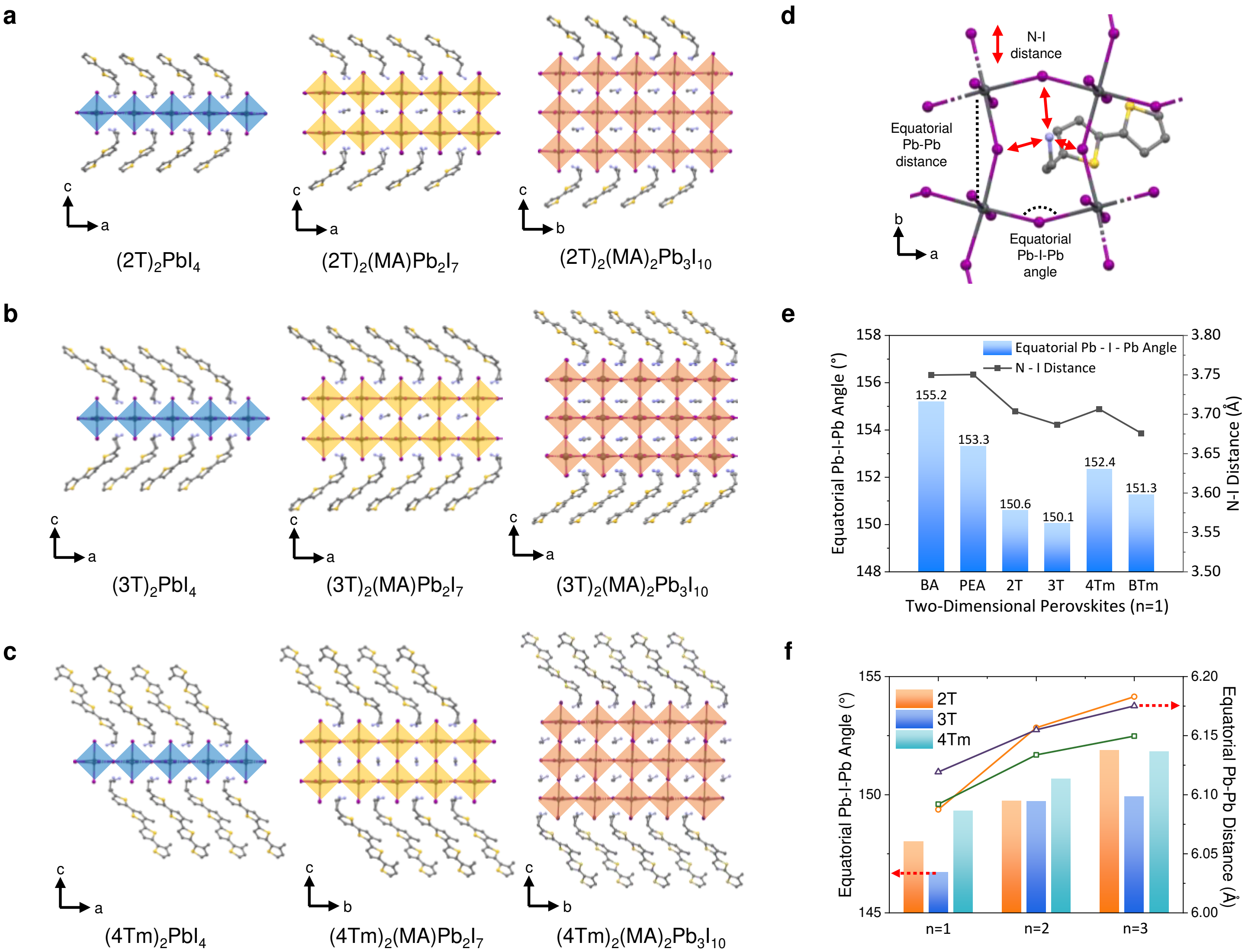

a
(2T)$_2$PbI$_4$
(2T)$_2$(MA)Pb$_2$I$_7$
(2T)$_2$(MA)$_2$Pb$_3$I$_{10}$
b
(3T)$_2$PbI$_4$
(3T)$_2$(MA)Pb$_2$I$_7$
(3T)$_2$(MA)$_2$Pb$_3$I$_{10}$
c
(4Tm)$_2$PbI$_4$
(4Tm)$_2$(MA)Pb$_2$I$_7$
(4Tm)$_2$(MA)$_2$Pb$_3$I$_{10}$
d
N-I distance
Equatorial Pb-Pb distance
Equatorial Pb-I-Pb angle
e
Equatorial Pb - I - Pb Angle
N - I Distance
Equatorial Pb-I-Pb Angle (°)
N-I Distance (Å)
155.2
153.3
150.6
150.1
152.4
151.3
BA
PEA
2T
3T
4Tm
BTm
Two-Dimensional Perovskites (n=1)
f
2T
3T
4Tm
Equatorial Pb-I-Pb Angle (°)
Equatorial Pb-Pb Distance (Å)
n=1
n=2
n=3

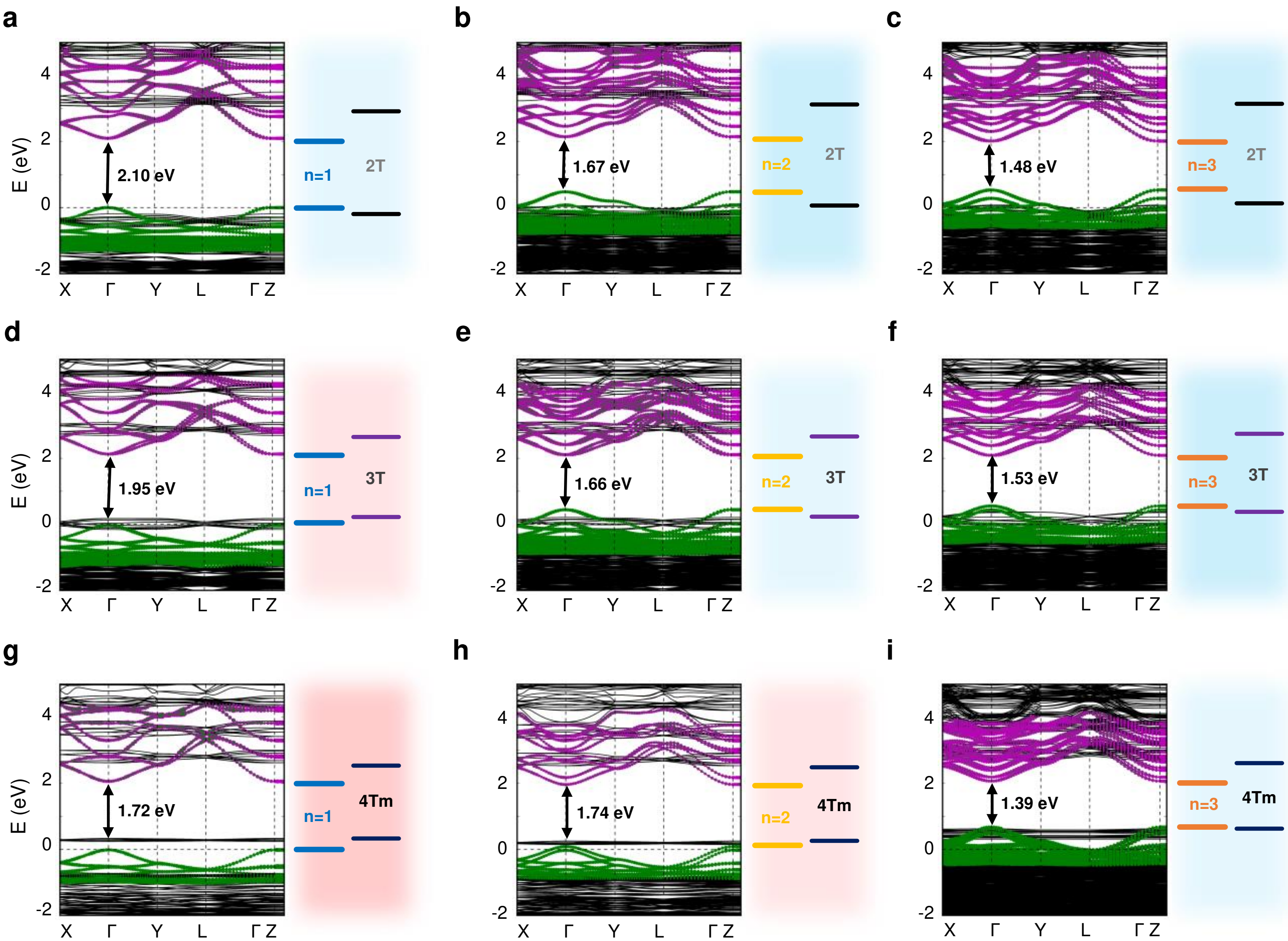

a
b
c
d
e
f
g
h
i
E (eV)
X Γ Y L Γ Z
2.10 eV
1.67 eV
1.48 eV
1.95 eV
1.66 eV
1.53 eV
1.72 eV
1.74 eV
1.39 eV
n=1
n=2
n=3
2T
3T
4Tm

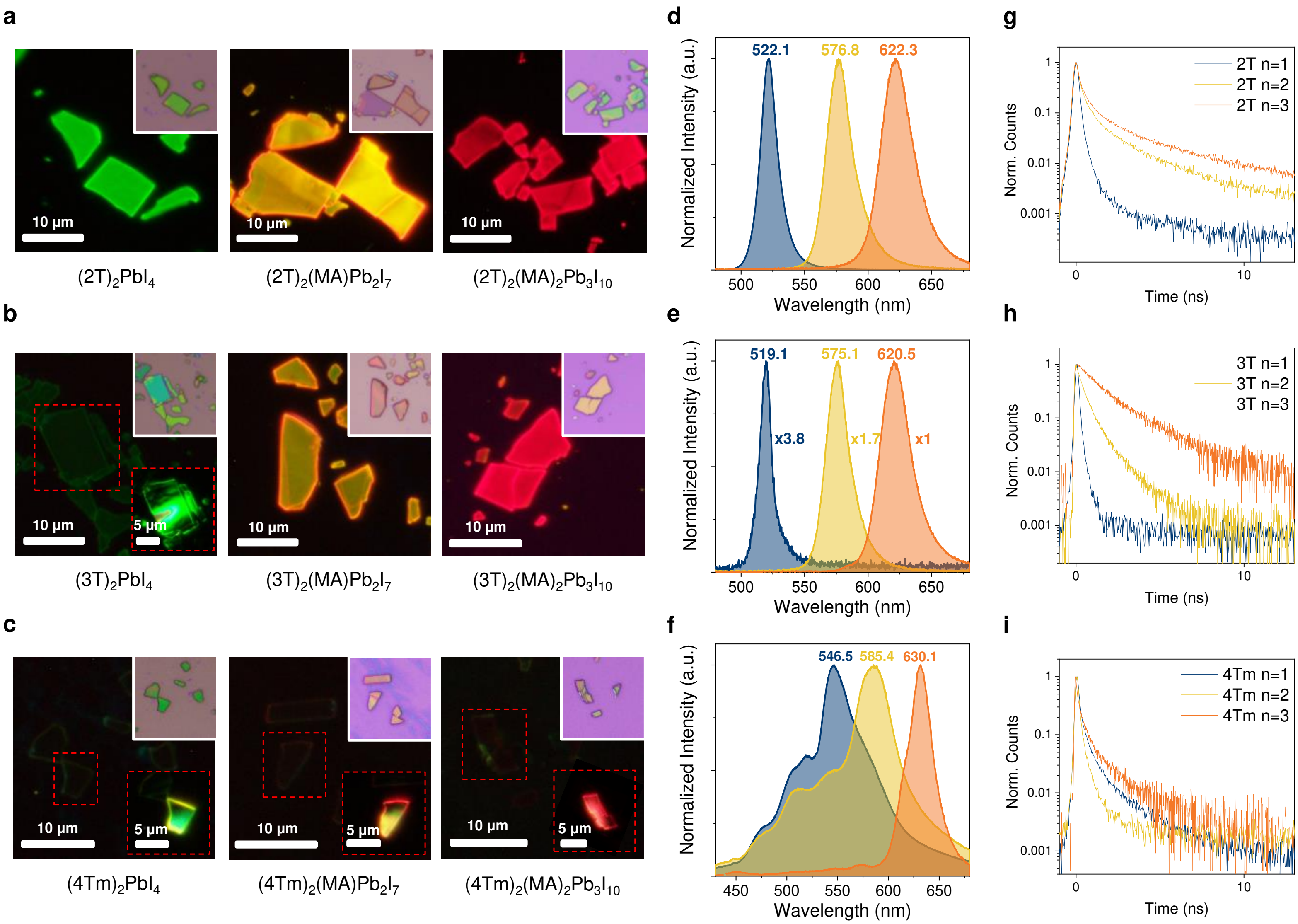

a
b
c
d
e
f
g
h
i
10 µm
5 µm
(2T)2PbI4
(2T)2(MA)Pb2I7
(2T)2(MA)2Pb3I10
(3T)2PbI4
(3T)2(MA)Pb2I7
(3T)2(MA)2Pb3I10
(4Tm)2PbI4
(4Tm)2(MA)Pb2I7
(4Tm)2(MA)2Pb3I10
522.1
576.8
622.3
519.1
575.1
620.5
x3.8
x1.7
x1
546.5
585.4
630.1
Normalized Intensity (a.u.)
Wavelength (nm)
2T n=1
2T n=2
2T n=3
3T n=1
3T n=2
3T n=3
4Tm n=1
4Tm n=2
4Tm n=3
Norm. Counts
Time (ns)

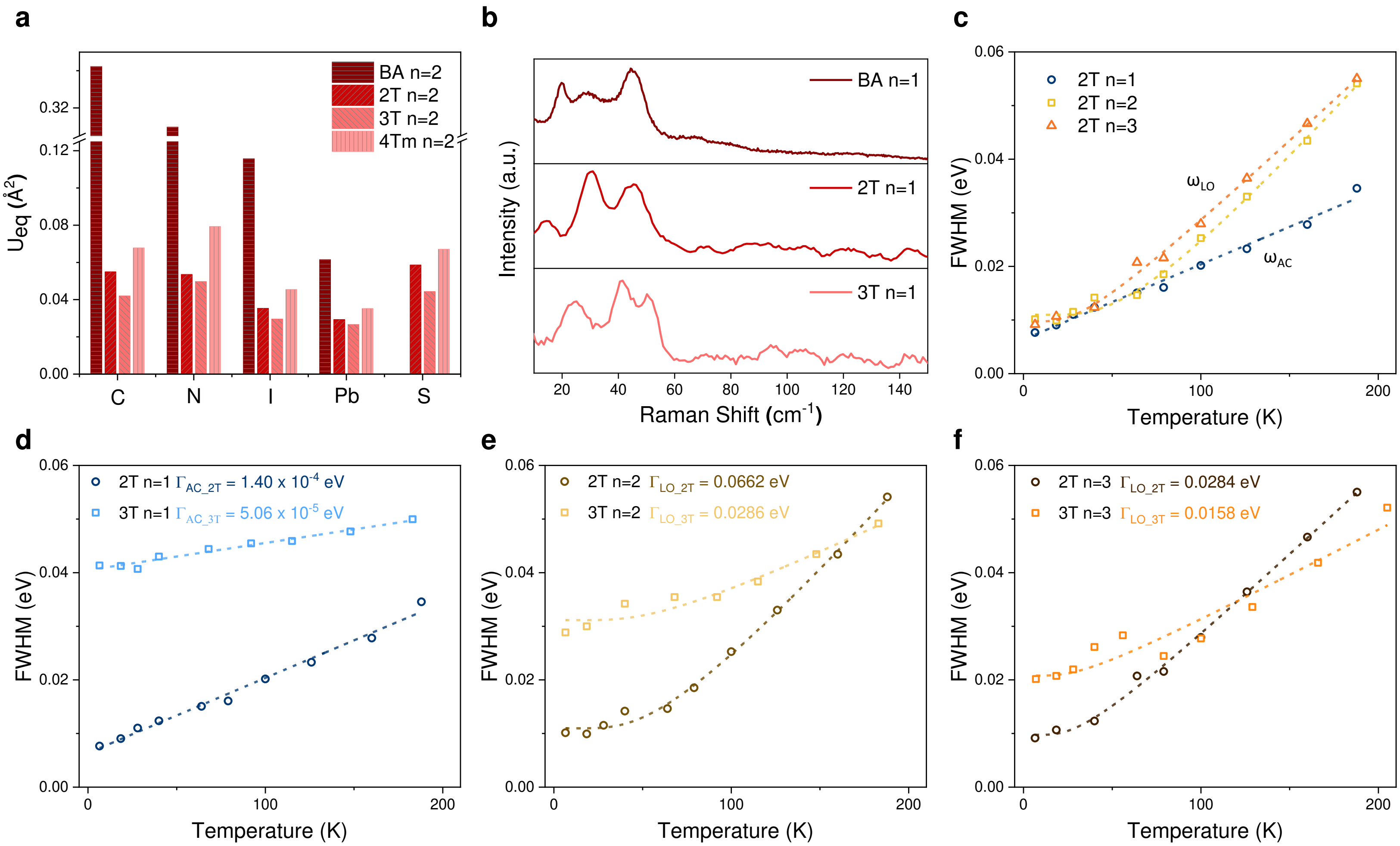
a
b
c
d
e
f
BA n=2
2T n=2
3T n=2
4Tm n=2
Ueq (Å2)
C
N
I
Pb
S
BA n=1
2T n=1
3T n=1
Intensity (a.u.)
Raman Shift (cm-1)
2T n=1
2T n=2
2T n=3
ωLO
ωAC
FWHM (eV)
Temperature (K)
2T n=1 ΓAC_2T = 1.40 x 10-4 eV
3T n=1 ΓAC_3T = 5.06 x 10-5 eV
2T n=2 ΓLO_2T = 0.0662 eV
3T n=2 ΓLO_3T = 0.0286 eV
2T n=3 ΓLO_2T = 0.0284 eV
3T n=3 ΓLO_3T = 0.0158 eV

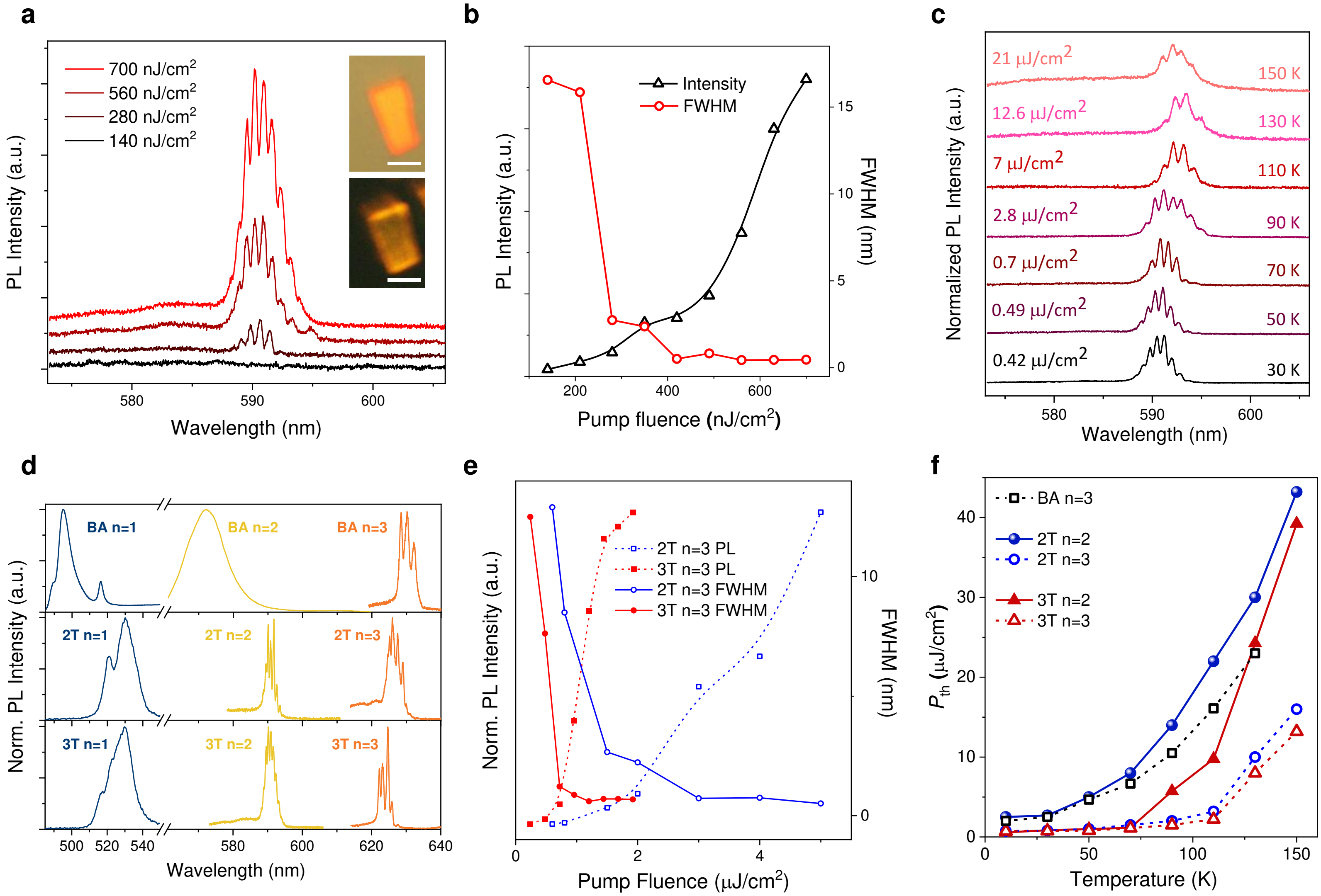
a
700 nJ/cm2
560 nJ/cm2
280 nJ/cm2
140 nJ/cm2
PL Intensity (a.u.)
Wavelength (nm)
b
Intensity
FWHM
PL Intensity (a.u.)
FWHM (nm)
Pump fluence (nJ/cm2)
c
21 μJ/cm2
150 K
12.6 μJ/cm2
130 K
7 μJ/cm2
110 K
2.8 μJ/cm2
90 K
0.7 μJ/cm2
70 K
0.49 μJ/cm2
50 K
0.42 μJ/cm2
30 K
Normalized PL Intensity (a.u.)
Wavelength (nm)
d
BA n=1
BA n=2
BA n=3
2T n=1
2T n=2
2T n=3
3T n=1
3T n=2
3T n=3
Norm. PL Intensity (a.u.)
Wavelength (nm)
e
2T n=3 PL
3T n=3 PL
2T n=3 FWHM
3T n=3 FWHM
Norm. PL Intensity (a.u.)
FWHM (nm)
Pump Fluence (μJ/cm2)
f
BA n=3
2T n=2
2T n=3
3T n=2
3T n=3
Pth (μJ/cm2)
Temperature (K)

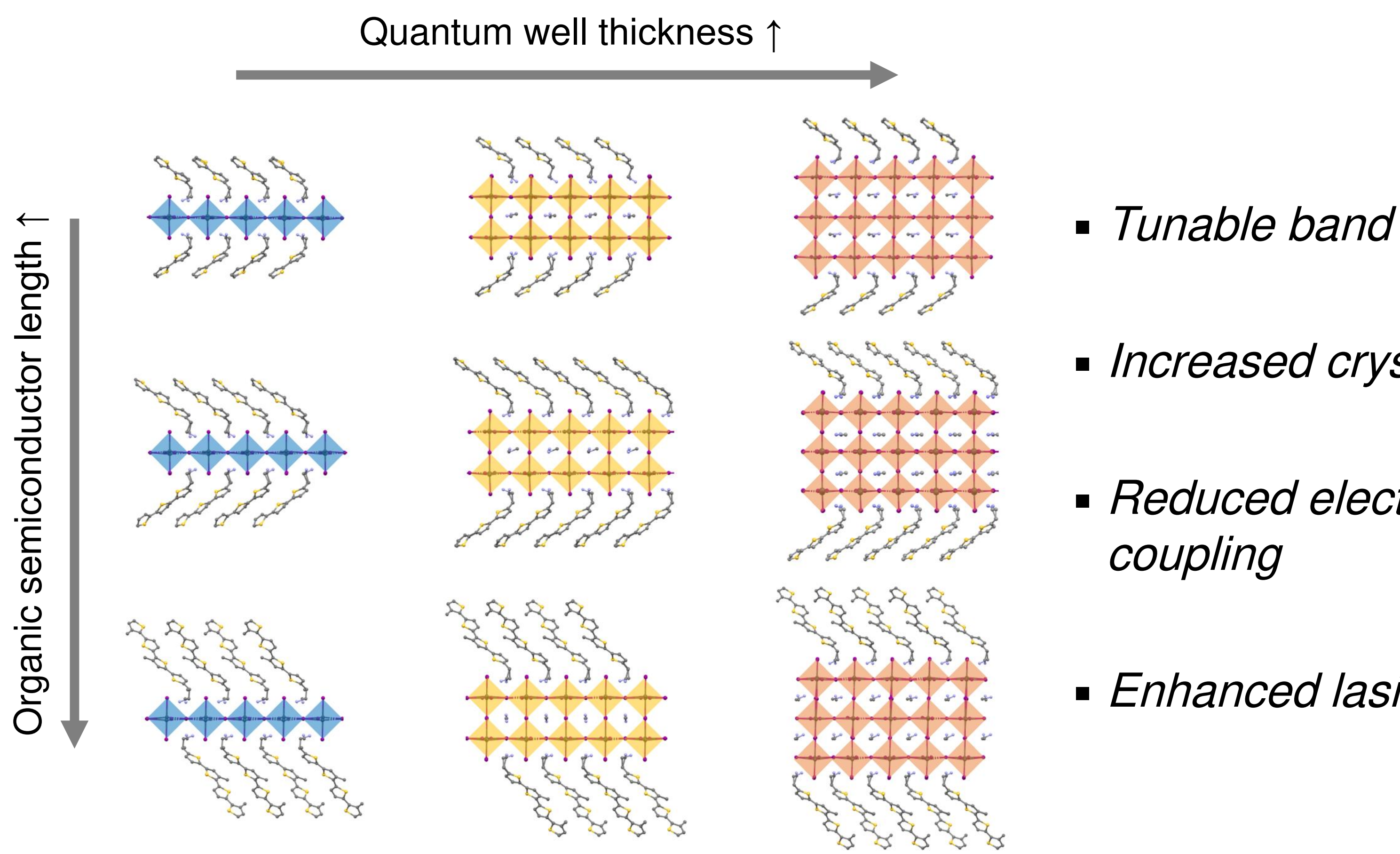
Quantum well thickness ↑
Organic semiconductor length ↑
Tunable band
Increased crys
Reduced elect
coupling
Enhanced lasi